A NOVEL SYSTEM FOR THE COMBINED MEASUREMENT OF WAVE- AND FLOW-FIELDS BENEATH WIND INDUCED WATER WAVES

Frank Hering Günther Balschbach Bernd Jähne

Interdisciplinary Center for Scientific Computing
University of Heidelberg
Im Neuenheimer Feld 368
D-69120 Heidelberg
Federal Republic of Germany
fhering@giotto.iwr.uni-heidelberg.de

Institute for Environmental Physics
University of Heidelberg
Im Neuenheimer Feld 366
D-69120 Heidelberg
Federal Republic of Germany

Commision V, Working Group V/III

KEY WORDS: Camera,Optical,Sensor,Underwater,Experiment

ABSTRACT

At the same time and location, simultaneous time series of wave slope images and the flowfield beneath water waves were obtained using an integrated set-up including particle-tracking and wave slope instruments. By an especially developed tracking algorithm, hundreds of seeding particles can be traced automatically, measuring the flow field. At the the same location the wave-field was measured with an illumination technique based on shape-from-refraction. Simultaneous flow- and wave-field measurements allow the investigation of transport processes across the water surface.

1 INTRODUCTION

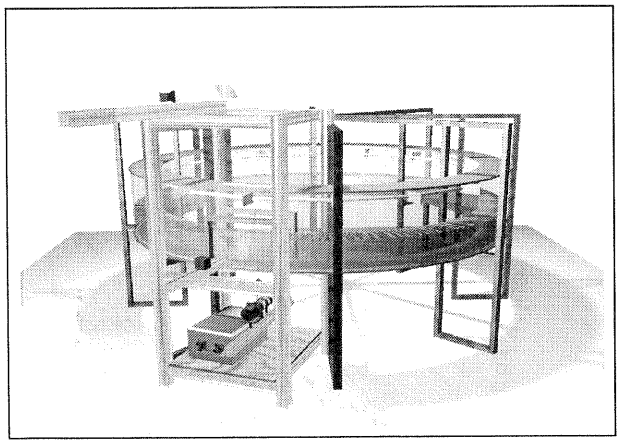

Figure 1: *Experiments were conducted at the circular wind/wave facility (perimeter 11.6 m, width 0.3 m, water depth 0.3 m) of the Institute for Environmental Physics of the University of Heidelberg (Germany).*

In this paper a novel optical technique is described that combines two spatially measuring systems in one setup: wave slope imaging and flow visualization. Both systems have already been used individually for some time, but are now put together for the first time. The wave visualization provides all relevant parameters of the water wave: the local wave number, the frequency, and the phase speed as a function of the phase and amplitude of the long waves [Balschbach et al., 95]. From the flow field measurements, similar information is gained for the orbital velocities. In addition, two dimensional velocity fields and later vorticity fields can be derived, yielding mass flux and Reynolds stresses [Hering, 96]. The aim of this paper is to describe the imaging techniques for simultaneous flow field and wave measurements. The instruments were mounted at Heidelbergs circular wind/wave facility, see Fig. 1.

2 PARTICLE TRACKING

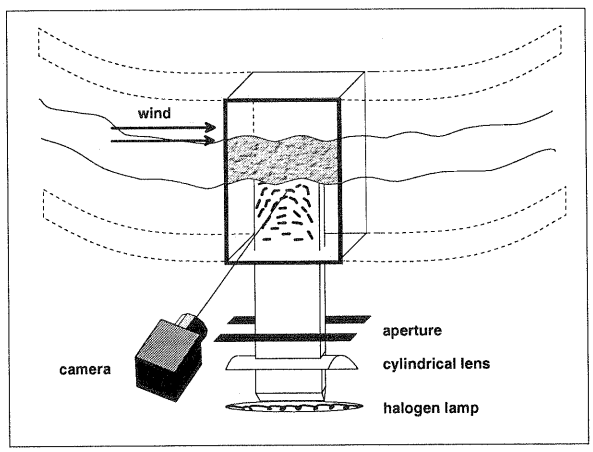

Figure 2: *Scheme of the optical instrument as used for Particle Tracking. Due to the integration time of the camera tracer particles in the light sheet are visualized as streaks.*

Particle Tracking Velocimetry (PTV) was chosen as a tool for the investigation of wave generated turbulences and turbulent transport. The flow field was visualized by small polystyrol particles in a light sheet illumination. The particles are imaged by a CCD camera as streaks. By tracking individual particle streaks from one frame to the next the Lagrangian vector field (trajectories, particle path) is extracted.

A 1-3 cm thick light sheet parallel to the main wave propagation direction is used to illuminate small (50-150 μm in diameter) polystyrol (LATEX) seeding particles. The depth of the light sheet was chosen such that the particles stay in the illuminated area long enough to enable tracking. The light sheet is typically generated from below of the channel by Halogen lamps. An area of typically $14.0 \times 10.0\,\mathrm{cm}^2$ is imaged by a digital 200 Hz CCD camera (DALSA CA-DA-0256) with a spatial resolution of 256 by 256 pixels. Due to the movement of the particles during the exposure time of $\frac{1}{200}$ ms, they are imaged as streaks. The image sequences are stored on CD-Rom for later processing.

2.1 The Tracking Algorithm

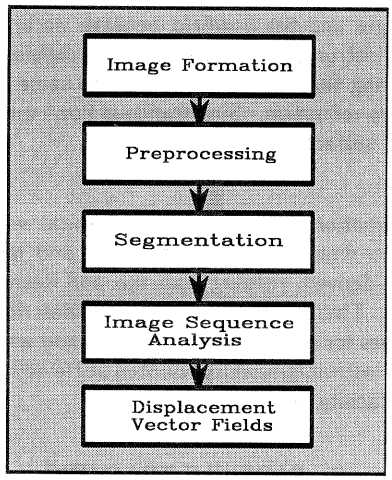

Figure 3: *An overview over the different steps of image processing, required for the evaluation of the vector field.*

Several image processing steps are required for the extraction of the flow field from the image sequences (see also Fig. 3). First the particle streaks are segmented by a specially developed segmentation technique. Each object is labeled and finally the correspondence problem of identifying the same object in the next image frame is solved by calculating its streak overlap. Repeating this algorithm will track segmented particles through the image sequence. Details can be found in [Hering et al.,95a].

Segmentation The histogram (Fig. 4) of a a streak image shows two distinct maxima, at the low gray values being faint particle streaks and the background and at high gray values being reflections at the water surface and bright particles. Therefore the intensity of the streaks ranges from the very low to the very high gray value. Simple pixel based segmentation techniques cannot be chosen as the streak images do not show a true bimodal distribution in the histogram. A region growing algorithm was developed for the discrimination of individual particles from the background. Regions with

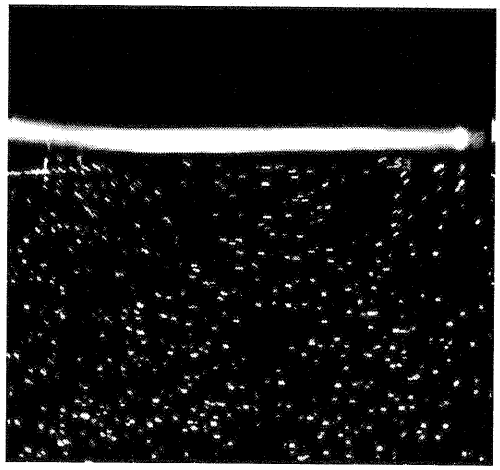

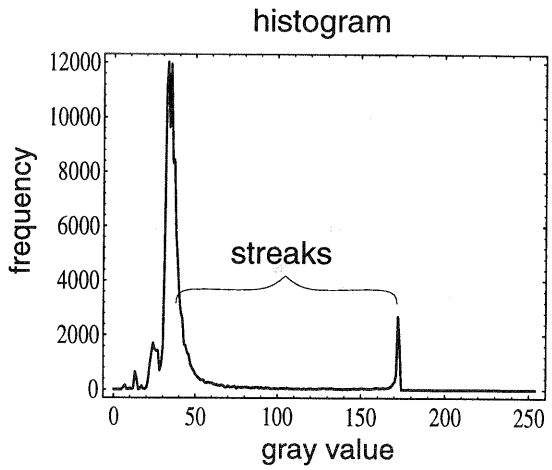

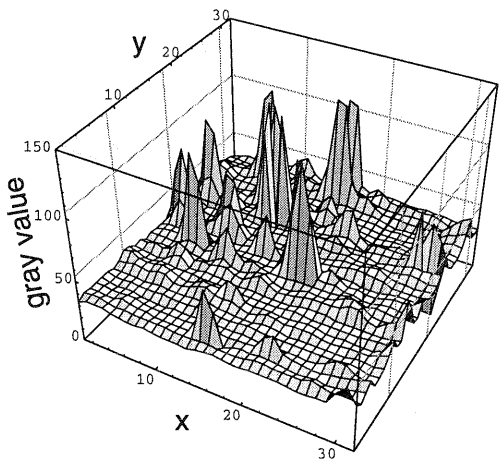

Figure 4: *Top: Original gray value image of polystyrol seeding particles beneath the water surface. An area of $14.0 \times 10.0\,\mathrm{cm}^2$ is imaged. Middle: Histogram of the above streak image. Although appearing to show a bimodal distribution, particles cannot be segmented by a threshold. Bottom: Pseudo 3d-plot of 32×32 pixels of the original streak image. Streaks can clearly be identified as local maxima in the gray value distribution.*

similar features are to be identified and merged together to a connected object.

Firstly the image g(x,y) is scanned through for local maxima

in the intensity, as the location of streaks is well approximated by a local maximum $g_{max}(x,y)$ (Fig. 4). A minimum search horizontally and vertically from $g_{max}(x,y)$ enables the calculation of the peak height:

$$\Delta g \quad = \quad \min(g_{max} - g_{min,i}) \,, \qquad (1)$$

$g_{min,i}$ being the minima revealed by the minimum search. In addition the half width is measured. Both peak height and half width are required to lie above a threshold to prevent random noise being a seeding point for the region growing. After these germ points are identified the growing algorithm segments the object following two rules: Firstly, a pixel is accepted as an object point only when its gray value is higher than an adaptive threshold, which is calculated from $g_{min,i}$ by interpolation. For details regarding computation the threshold see [Hering et al., 95b]. Secondly only those pixels forming a connected object are considered. A result of the described segmentation algorithm is shown in Fig. 5. Each object identified by the segmentation is then labeled with a flood fill algorithm borrowed from computer graphics. The size of each object can then be determined, and thereby large objects (reflections at the water surface) removed.

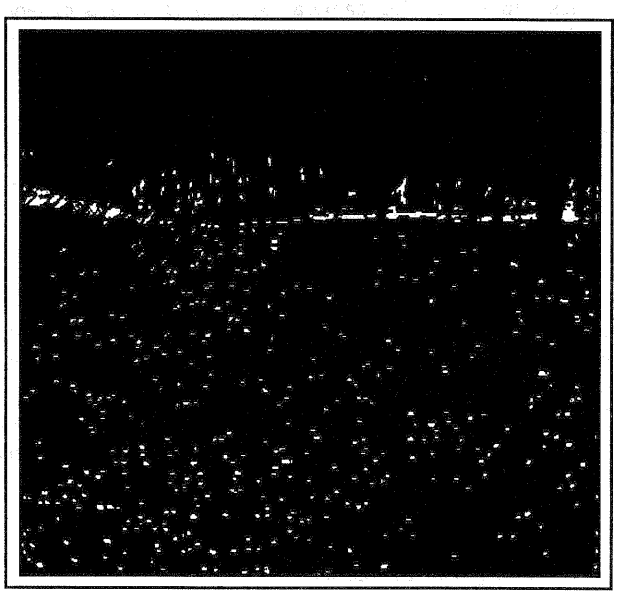

Figure 5: *Segmented image of original gray value picture (Fig. 4 top). 501 objects were found. The reflections at the water surface were eliminated by the labeling algorithm.*

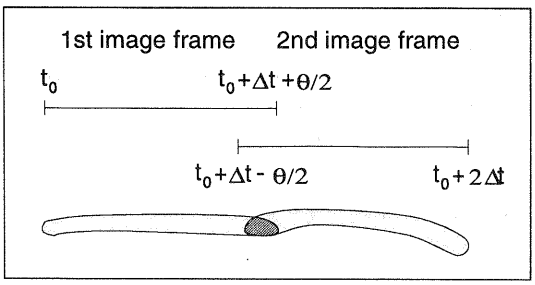

Figure 6: *The temporal overlap θ of the exposure time in two consecutive fields of the same frame yields a spatial overlap of corresponding streaks.*

Image Sequence Analysis After segmentation, the correspondence problem of identifying the same particle in the next image frame is solved, by calculating its image field streak overlap: Some cameras (e.g the Pulnix TM640) show a significant overlap θ of the exposure in two consecutive fields of the same frame. The overlap of the exposure time yields a spatial overlap of the two corresponding streaks from one image to the next (Fig. 6). An AND operation between two consecutive segmented fields calculates the overlap fast and efficiently [Hering et al.,95a]. In addition as the temporal order of the image fields is known, the sign of the vector is also known and no directional ambiguity has to be solved. However most cameras do not show such a temporal overlap in the exposure time. In these cases corresponding particles will only overlap due to their expansion in space. Artificially this expansion can be increased by the use of a morphological dilation operator. The binary dilation operator of the set of object points $\mathcal{O}$ by a mask M is defined by:

$$\mathcal{O} \oplus M = \{p : \; M_p \cap \mathcal{O} \neq \emptyset\} \,, \qquad (2)$$

where M_p denotes the shift of the mask to the point p, in that way that p is localized at the reference point of the mask. The dilation of $\mathcal{O}$ by the mask M is therefore the set of all points, where the intersecting set of $\mathcal{O}$ and M_p is not empty. This operation will enlarge objects and typically smooth their border. For more details see [Jähne, 95]. To avoid unnecessary clustering of the objects the dilation is not calculated simultaneously for all objects in an image but for each object individually. In most cases, in particular for low particle concentration(≤ 300 particles/image), each particle shows only the overlap with the corresponding particle in the next frame. At higher particle concentration, particles however show overlap with up to typically four particles in the next frame. Therefore additional features are required to minimize false correspondences. Ideally the sum of gray values for each streak in the image series should be constant, due to the equation of continuity for gray values [Hering, 96]:

$$\sum_{x,y \in \mathcal{O}} g(x,y) \;=\; \text{const.}sigma \,. \qquad (3)$$

This implies a particle at low speed is visualized as a small bright spot. The same particle at higher speed is imaged as a fainter object extending over a larger area. The sum of gray values in both cases should be identical. Deviations from this ideal situation are caused by segmentation errors. Better results are therefore gained by normalizing the sum of gray values with the segmented area. The normalized sum of gray values being G_n^1 for the first frame and G_n^2 for the second are required to lie above a threshold of the confidence interval C:

$$C \quad = \quad 1 - \frac{|G_n^1 - G_n^2|}{|G_n^1 + G_n^2|} \quad \longmapsto \quad [0,1] \,. \qquad (4)$$

A similar expression can be derived for the area of the objects. Finally the expected position of a particle is predicted by interpolation, from the vector field of previous time steps [Hering et al., 95b]. A χ^2-test evaluates the probability that a pair of particles match. Minimizing χ^2 will maximize the likelihood function.

Calculation Of The Displacement Vector Field [Hering, 96] showed that the center of gray value $\vec{x}_c$

of an isotropic object represents the timely averaged two dimensional location $\langle \vec{x} \rangle_{\Delta t}$, thus:

$$\vec{x}_c = \langle \vec{x} \rangle_{\Delta t} \ , \tag{5}$$

where $\vec{x}_c$ is calculated from the sum of all n segmented pixels of a streak:

$$\vec{x}_c = \left(\frac{\sum_{i=1}^{n} x_i g(x_i, y_i)}{\sum_{i=1}^{n} g(x_i, y_i)} \ , \ \frac{\sum_{i=1}^{n} y_i g(x_i, y_i)}{\sum_{i=1}^{n} g(x_i, y_i)} \right) . \tag{6}$$

Now the knowledge of the location of the same particle in the previous frame (at the time $t-1$) enables the first-order approximation the velocity field $\vec{u}(t)$:

$$\vec{u}(t) \approx \frac{\vec{x}_c(t) - \vec{x}_c(t-1)}{\Delta t} . \tag{7}$$

Repeating the described algorithm will automatically track all encountered seeding particles from one frame to the next. The segmentation and tracking algorithms have been implemented on an i860 board to achieve maximum performance. Typical evaluation time of one image including digitization, segmentation and tracking is $10\,s$. Long image sequences (200-1000) images can therefore be processed. Individual particles can be tracked up to a concentration of 1000 particles/image.

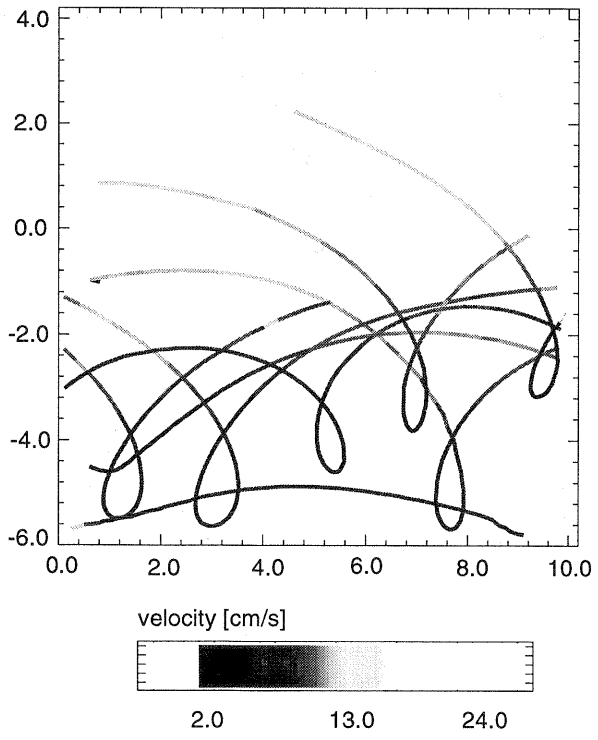

Figure 7: *Trajectories of tracer particles measured by the PTV-algorithm. Only a small fraction (less than 1 %) of all trajectories plotted. The velocities are encoded as intensity.*

3 COLOR IMAGING SLOPE GAUGE

Measurements of the spatial variations of the water surface slope at Heidelbergs wind/wave facility performed using a Color Imaging Slope Gauge (CISG).

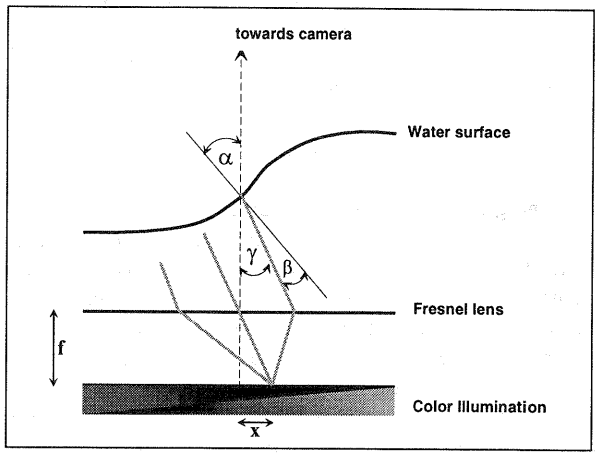

Figure 8: *Rays refracted under the same angle (same surface slope) are focused on one point of the screen, independent of the position on the surface and the water height. The slope of the waves is imaged.*

Figure 8 shows the schematic setup of the *imaging slope gauge* which was first proposed by [Jähne et al., 94] using a black and white CCD camera. A CCD camera is observing the water surface from far above. Therefore all the rays that enter the camera are nearly vertical i. e. perpendicular to a flat water surface. A single light emitting point on the screen at the bottom of the system is in the rear focal plane of a Fresnel lens. Therefore all rays emitted are parallel in the water. This spot can be seen on an image pixel, if the refraction for the corresponding point at the surface leads to a vertical beam in the air. So each pixel of the CCD sees a certain point of the screen, depending on the slope of the corresponding imaged surface element. With an intensity or color pattern on the screen, the slope of the imaged water surface is encoded in gray value or color information respectively.
The relation between surface slope $s = \tan(\alpha)$ at a certain point and the color imaged in the related pixel is independent of:

- the location at the surface and
- the height of the surface

Rays crossing different locations on the surface (or at different heights) with the same slope have the same angle of refraction and are therefore focused on the same screen point, imaging the same color (see fig. 8). Analyzing the color information in the digitized image, for each pixel the slope of the corresponding location on the water surface can be computed. One of to major advantages using this color technique instead of the black and white one previously used is that both slope components (streamwise and spanwise) are measured simultaneously.

3.1 Energy of Capillary Waves

Of especial importance for the process of air/sea interaction is the determination of the mean energy of a wave. According to [Phillips, 80] the energy E_c of a capillary wave with slope $\vec{s}$ is given by:

$$E_c = \frac{\sigma}{\rho} \|\vec{s}(x,y)\|^2 , \tag{8}$$

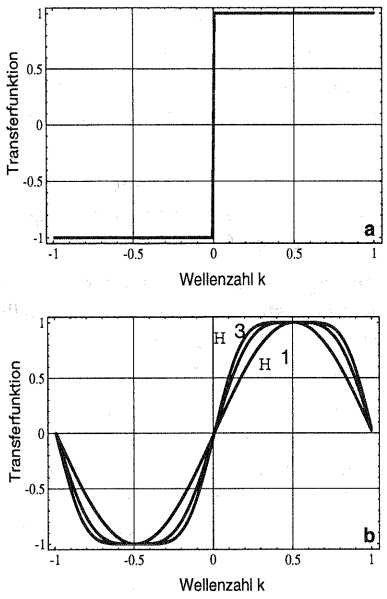

Figure 9: *Imaginary part of the transfer function of an optimal Hilbert filter (a), transfer function of the approximations (b) ${}^1\mathcal{H}$, ${}^2\mathcal{H}$ and ${}^3\mathcal{H}$ (see text).*

sigma denoting the surface tension and ρ the density of water. The wave energy was calculated from the wave slope images using a multi-scale Hilbert transformation technique. A Hilbert filter converts a signal in its Hilbert transform. It does not change the amplitude of the different spectral components, but shifts their phase by $\pi/2$. Therefore the magnitude of the transfer function is one [Jähne, 93]. Because of the $\pi/2$ phase shift, the transfer function is purely imaginary, of odd symmetry, jumping from $-i$ to i at the wavenumber $k = 0$, see Figure 9. The starting point for the design of a Hilbert filter is the observation that the convolution kernels of a first-order derivative operator (${}^1\mathcal{H}$ of figure 9) is odd and shows already the main features of a Hilbert filter. For the construction of better approximations a series of sine functions with odd wave number is expanded at $|k| = \frac{1}{2}$, yielding (see [Jähne, 93]):

$$
\begin{aligned}
{}^1\mathcal{H} &= \frac{1}{2}[1\ \ 0\ \ -1] \\
{}^2\mathcal{H} &= \frac{1}{16}[1\ \ 0\ \ 9\ \ 0\ \ -9\ \ 0\ \ -1] \\
{}^3\mathcal{H} &= \frac{1}{256}[3\ \ 0\ \ 25\ \ 0\ \ 150\ \ 0\ \ -150\ \ 0\ \ -25\ \ 0\ \ -3]
\end{aligned}
\tag{9}
$$

The transfer functions of theses three Hilbert filters are shown in Fig. 9. Simulations have shown, that these ordinary filters are only able to transfer a signal in its Hilbert-transform in a limited bandwidth from 2.5 to 10 pixels. Therefore all images were bandpass decomposed by a Laplace pyramid [Burt und Adelson, 83]. On each level of the pyramid the Hilbert transform can be computed effectively. By this multi-grid approach structures with wavenumbers from 2.5 to 40 pixels can be phase shifted effectively. Fig. 10 shows the energy extraction algorithm on a ring test pattern.

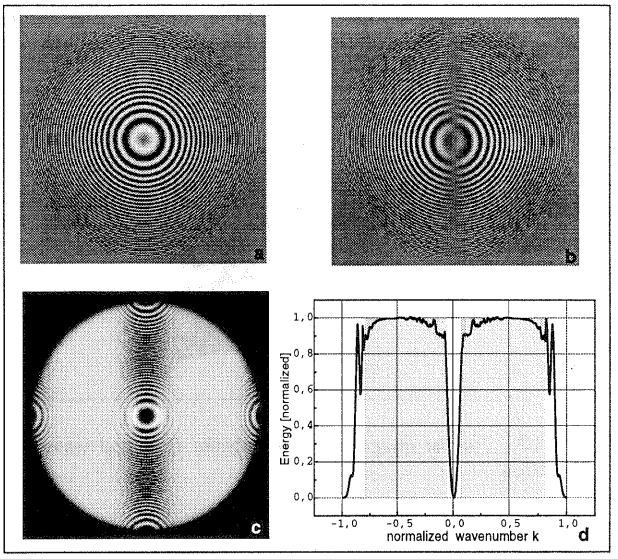

Figure 10: *Test ring pattern (a), Hilbert transformation (b), Energy of test pattern (c), energy profile (d).*

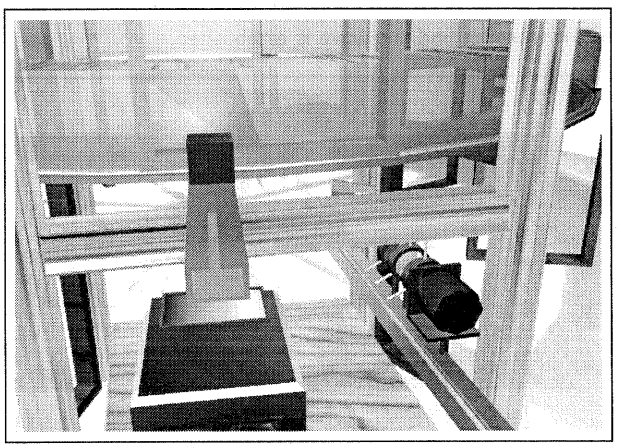

Figure 11: *Sketch of the integrated flow- and wave visualization set-up. One camera is observing the waves from above, a second camera is looking from the side on a light-sheet, visualizing seeding particles.*

4 SIMULTANEOUS FLOW- AND WAVE-VISUALIZATION

Due to the presence of the color wedge of the wave visualization the light sheet (flow visualization) cannot be generated from below of the channel. Thus it is produced from the sides of the wave visualization and then coupled into the channel through a prism (see Fig. 11). An optical system consisting of a spherical lens ($f = 200\,\text{mm}$) and a cylinder lens ($f = 90\,\text{mm}$) generates the light sheets. An immersion oil as an optical coupling medium links the prisms with the bottom window of the channel. As shown in Fig. 1 two illumination systems are combined to increase intensity and homogeneity in the image sector of $17 \times 20\,\text{cm}^2$. The oblique illumination angle has been chosen so that most of the light is totally reflected at the water surface. Only in rare cases - for steep waves - the light is refracted in such a way at the water surface that bright spots are observed in camera 1 for the wave slope imaging. This residual interference was eliminated by a blue Corion interference short wave pass filter (cut-off wave-

length $\lambda = 550\,\text{nm}$) in the light beam of the Xenon arc lamp and a red Schott glass filter (cut-on wavelength $\lambda = 600\,\text{nm}$) on camera 1 (Fig. 12).

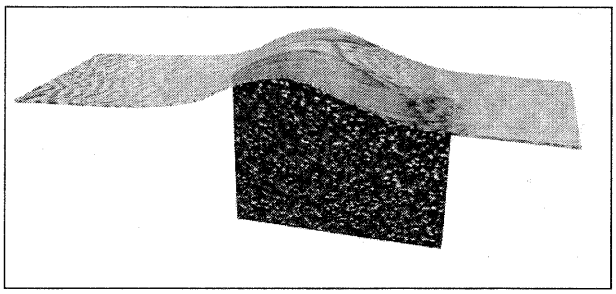

Figure 12: *Typical image of the combined flow and wave-field visualization.*

5 RESULTS

The combined flow- and wave-visualization allows the study of transport processes near the water surface. Fig. 13 shows three consecutive images taken $\frac{1}{200}$ s apart of breaking wave. Energy is transported from the wave-field to flow-field, a turbulent wake behind the wave is established.

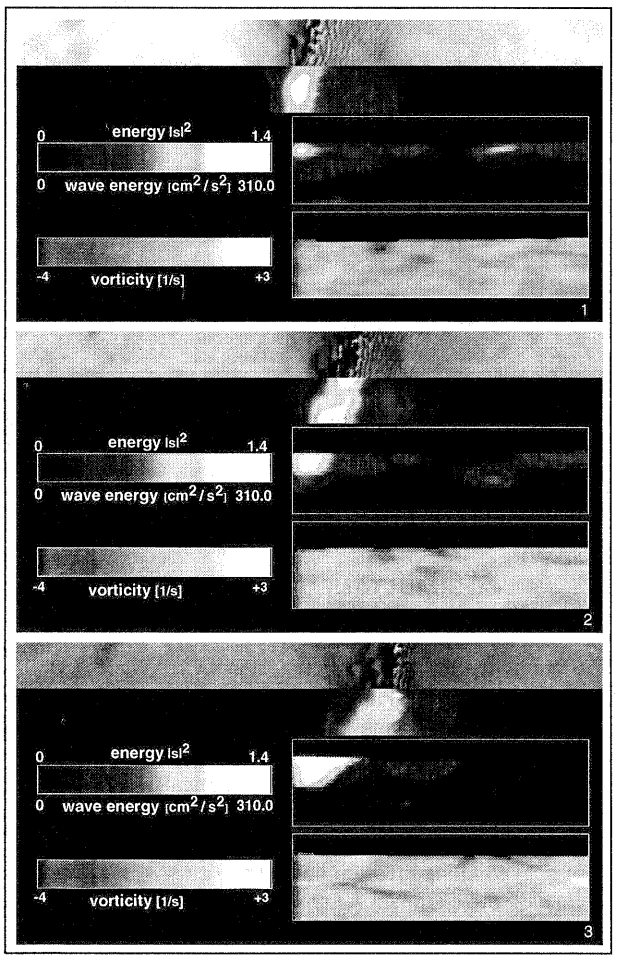

Figure 13: *Sequence of the simultaneously measured wave- and flowfield. For each time step: First stripe shows original wave slope image, second the energy extracted from wave images, third the energy in the flowfield, and fourth the vorticity. Due to wave breaking energy is transported from the wave field to the flow field.*

REFERENCES

[Balschbach et al., 95] Balschbach, G., Menzel, M. und Jähne, B., 1995. A New Instrument to Measure Steep Wind-Waves, presented at IAPSO, XXI General Assembly, Hawaii, to be published

[Burt und Adelson, 83] Burt, P.J. and Adelson E.H., 1983. The Laplacian pyramid as a compact image code , IEEE Trans. COMM, **31**, pp. 532-540.

[Hering, 96] Hering, F., 1996. Lagrangesche Untersuchungen des Strömungsfeldes unterhalb der wellenbewegten Wasseroberfläche mittels Bildfolgenanalyse, dissertation-thesis, Universität Heidelberg.

[Hering et al., 95b] Hering, F., Wierzimok, D., and Jähne B., 1995. Particle Tracking in Space Time Sequences, Proc. of 6th International Conference on Computer Analysis of Images and Patterns, CAIP'95, Prague, September 6-8, in Lecture Notes in Computer Science, Vol. **970**, Springer Verlag, Berlin.

[Hering et al.,95a] Hering, F., Merle, M., Wierzimok, D., and Jähne B., 1995. A Robust Technique for Tracking Paricles over Long Image Sequences, Proc. of ISPRS Intercommission Workshop 'From Pixels to Sequences', Zurich, March 22-24, in International Archives of Photogram. and Remote Sensing , Vol. **30**, Part 5W1.

[Jähne, 95] Jähne, B., 1995. Digital Image Processing, Springer Verlag, 3rd edition.

[Jähne et al., 94] Jähne, B., Klinke J. and Waas, S., 1994. Imaging of short ocean wind waves: a critical review, Journal of the Optical Society of America A, Vol. **11**, No. 8, pp. 2197-2209.

[Jähne, 93] Jähne, B., 1993. Spatio-Temporal Image Processing, Lecture Notes in Computer Science, No.**751** Springer Verlag.

[Phillips, 80] Phillips, O.M., 1980. The Dynamics of the Upper Ocean, Cambridge University Press, New York.